

# Tectonophysics

## Slow slip events and flank instability at Mt. Etna volcano (Italy)

--Manuscript Draft--

<b>Manuscript Number:</b>	
<b>Article Type:</b>	Research Paper
<b>Keywords:</b>	slow slip event; unstable flank; distributed slip model; aseismic deformation; Mt. Etna
<b>Corresponding Author:</b>	Mimmo Palano, PhD Istituto Nazionale di Geofisica e Vulcanologia Catania, ITALY
<b>First Author:</b>	Mimmo Palano, PhD
<b>Order of Authors:</b>	Mimmo Palano, PhD Federica Sparacino Piera Gambino Nicola D'Agostino Stefano Calcaterra
<b>Abstract:</b>	<p>We analysed a set of 11 slow slip events occurred during the 2006-2016 period and affecting the GPS stations of the unstable flank of Mt. Etna volcano. Observed surface deformation for most of the detected slow slip events, concentrates on the south-eastern edge of the unstable flank while the slow slip events involving the north-eastern edge are less frequent. Such a feature highlights the existence of two distinct families of events, involving two contiguous sectors of the unstable flank, which occasionally slip together in large slow slip events. The modelled slips also highlight that both contiguous sectors extend ~10-12 km off-shore, on areas where active tectonic lineaments such as the ESE (northward of Catania Canyon) and the N102° (along the southern slope of the Riposto Ridge) ones have been recently discovered. Equivalent seismic moments of slow slip events occurred in the last ten years (corresponding to magnitudes in the range 5.4-5.9) are larger than those associated to seismic events observed in the last 200 years, suggesting that most of the deformation affecting the eastern flank occurs aseismically.</p>
<b>Suggested Reviewers:</b>	Kristy Tiampo kristy.tiampo@colorado.edu Expert on geodesy and data modelling  Matteo Lupi matteo.lupi@unige.ch Expert on volcanoes  José Fernández Torres jft@mat.ucm.es Expert on geodesy and data modelling  Yo Fukushima yofukushima@rcep.dpri.kioto-u.ac.jp

Dear Editor

We are very pleased to submit our manuscript entitled “Seismic and geodetic moment-rates comparison for the Aegean - Anatolian region” in order to be considered for publication in **Tectonophysics**.

The manuscript focuses on a sequence of slow slip events occurring at Mt. Etna since early 2006. Such a kind of aseismic events have been detected at a variety of tectonic and volcanic areas in the last decade, capturing the curiosity of seismic and geodetic communities. Hence, this submission while is of timely significance, is also of broad interest. Moreover, it provides additional constraints about the seaward flank motion of Mt. Etna volcano.

We provide you a list of 5 potential reviewers, with wide range of expertise to judge this manuscript:

- Kristy Tiampo (University of Colorado) USA, [kristy.tiampo@colorado.edu](mailto:kristy.tiampo@colorado.edu)
- Maurizio Battaglia (Sapienza - Università di Roma), [maurizio.battaglia@uniroma1.it](mailto:maurizio.battaglia@uniroma1.it)
- Yo Fukushima, Kyoto University, Japan ([yofukushima@rcep.dpri.kyoto-u.ac.jp](mailto:yofukushima@rcep.dpri.kyoto-u.ac.jp))
- Matteo Lupi, University of Geneva, Switzerland ([matteo.lupi@unige.ch](mailto:matteo.lupi@unige.ch))
- José Fernández Torres, Instituto de Geociencias, SPAIN ([jft@mat.ucm.es](mailto:jft@mat.ucm.es))

We strongly believe that **Tectonophysics** is the best journal for sharing our efforts with the scientific community. For this reason, we really hope that you will find of interest our paper!

Yours sincerely

Mimmo Palano (on behalf all the authors)

## **Abstract**

We analysed a set of 11 slow slip events occurred during the 2006-2016 period and affecting the GPS stations of the unstable flank of Mt. Etna volcano. Observed surface deformation for most of the detected slow slip events, concentrates on the south-eastern edge of the unstable flank while the slow slip events involving the north-eastern edge are less frequent. Such a feature highlights the existence of two distinct families of events, involving two contiguous sectors of the unstable flank, which occasionally slip together in large slow slip events. The modelled slips also highlight that both contiguous sectors extend ~10-12 km offshore, on areas where active tectonic lineaments such as the ESE (northward of Catania Canyon) and the N102° (along the southern slope of the Riposto Ridge) ones have been recently discovered. Equivalent seismic moments of slow slip events occurred in the last ten years (corresponding to magnitudes in the range 5.4-5.9) are larger than those associated to seismic events observed in the last 200 years, suggesting that most of the deformation affecting the eastern flank occurs aseismically.



**Highlights** (three to five; 85 characters or fewer, including space)

- A set of slow slip events occurred at Mt. Etna volcano is analyzed
- Two distinct families of slow slip events have been detected
- Most of the deformation affecting the eastern flank occurs aseismically
- Different sources temporally modulate the seaward motion of the unstable flank

1                   **Slow slip events and flank instability at Mt. Etna volcano (Italy)**

2  
3           Mimmo Palano<sup>a\*</sup>, Federica Sparacino<sup>a</sup>, Piera Gambino<sup>b</sup>, Nicola D'Agostino<sup>c</sup>, Stefano Calcaterra<sup>b</sup>

4  
5  
6   <sup>a</sup> Istituto Nazionale di Geofisica e Vulcanologia, Sezione di Catania, Osservatorio Etneo, Catania 95125, Italy

7   <sup>b</sup> Italian Institute for Environmental Protection and Research (ISPRA), Rome 00144, Italy

8   <sup>c</sup> Istituto Nazionale di Geofisica e Vulcanologia, Osservatorio Nazionale Terremoti, Rome 00143, Italy

9  
10  
11  
12  
13  
14  
15  
16  
17  
18  
19  
20  
21  
22  
23  
24  
25  
26  
27  
28  
29   **\*Corresponding author:**

30   Mimmo Palano

31   Istituto Nazionale di Geofisica e Vulcanologia, Osservatorio Etneo - Sezione di Catania,

32   P.zza Roma 2, I-95123 Catania (Italy)

33   Phone: +39 0957165800

34   Email: mimmo.palano@ingv.it

35

36

37

38

## 39 **Abstract**

40 We analysed a set of 11 slow slip events occurred during the 2006-2016 period and  
41 affecting the GPS stations of the unstable flank of Mt. Etna volcano. Observed surface  
42 deformation for most of the detected slow slip events, concentrates on the south-eastern edge  
43 of the unstable flank while the slow slip events involving the north-eastern edge are less  
44 frequent. Such a feature highlights the existence of two distinct families of events, involving  
45 two contiguous sectors of the unstable flank, which occasionally slip together in large slow slip  
46 events. The modelled slips also highlight that both contiguous sectors extend ~10-12 km off-  
47 shore, on areas where active tectonic lineaments such as the ESE (northward of Catania  
48 Canyon) and the N102° (along the southern slope of the Riposto Ridge) ones have been recently  
49 discovered. Equivalent seismic moments of slow slip events occurred in the last ten years  
50 (corresponding to magnitudes in the range 5.4-5.9) are larger than those associated to seismic  
51 events observed in the last 200 years, suggesting that most of the deformation affecting the  
52 eastern flank occurs aseismically.

53

54

55 **Keywords:** *slow slip event, unstable flank, distributed slip model, aseismic deformation, Mt.*  
56 *Etna*

57

## 58 **1.0 Introduction**

59 Episodic aseismic slip events are earthquake-like events which, releasing energy over  
60 a period of hours to months, have been detected at a variety of tectonic and volcanic  
61 environments. These particular events, termed as slow slip events (SSE hereinafter), are  
62 becoming increasingly recognized as important, due to their influence on local and regional  
63 seismicity. Indeed, recent studies have highlighted that the SSEs occur close to zones of  
64 frictional transition from velocity strengthening to velocity weakening (Liu and Rice, 2007;  
65 Rubin, 2011; Segall et al., 2010) therefore providing useful information on fault zone  
66 properties.

67 The first detected SSE dates December 1992 and occurred along the San Andreas fault  
68 in central California (Linde et al., 1996). This SSE was detected by two borehole strainmeters  
69 which were installed closely to the main fault and recorded a transient deformation event of  
70 about a week in duration. The rapid increase of continuous GPS (CGPS) stations has allowed  
71 to detected a large number of SSEs worldwide. The large majority of SSEs has been observed  
72 at convergent plate boundaries. Valuable examples come from Cascadia (Dragert et al., 2001;

73 2004; Brudzinski and Allen, 2007; Haines et al., 2019), New Zealand (Beavan et al., 2007) and  
74 Japan (Hirose et al., 1999; Obara and Hirose, 2006; Ito et al., 2013). Sometimes they are  
75 associated with seismic tremor (Dragert et al., 2001; 2004; Brudzinski and Allen, 2007; Haines  
76 et al., 2019; Beavan et al., 2007), but not exclusively. For example, it has long been recognized  
77 that detected SSEs in Cascadia are nearly always accompanied by seismic tremor (Rogers and  
78 Dragert, 2003), with a few exceptions for brief times during individual SSEs when slip appears  
79 to occur with no obvious tremor (Wech and Bartlow, 2014).

80 In the last two decades more than 10 SSEs have been identified from CGPS data at  
81 Kilauea volcano southern flank (see Foster et al., 2013 and references therein). These SSEs  
82 exhibit surface displacements up to a few centimeters, duration of several hours to 2 days and  
83 occur along the off-shore portion of the basal decollement (e.g. Montgomery-Brown et al.,  
84 2009).

85 The occurrence of SSEs has been detected also at Mt. Etna from the continuous GPS  
86 stations covering the continuous seaward moving eastern flank of the volcano (see Palano 2016  
87 and references therein for additional details). Here, taking into account a new set of GPS data  
88 acquired at the SiOrNet network (Figure 1) we improved the results reported in Palano (2016)  
89 by extending in time (back and forward) the preexisting SSE catalog. Moreover, we performed  
90 a new modelling of the surface deformation associated to each SSE in order to better constrain  
91 the slip distribution pattern on the causative source. Achieved results are discussed in the  
92 general setting of the eastern flank of the volcano, in order to provide an improved picture  
93 about its complex kinematics and block fragmentation.

94

## 95 **2.0 Mt. Etna background**

96 Mt. Etna is a basaltic Quaternary volcano located on the east coast of Sicily (South  
97 Italy) at the front of the Apennine-Maghrebian chain (AMC) (Figure 1). The volcano developed  
98 over the last 500 ka over metamorphic and sedimentary rocks (belonging to the AMC) on its  
99 western and northern slopes and over Quaternary plastic clays (accumulated along the Gela-  
100 Catania Foredeep at the front of AMC; Branca and Ferrara, 2013). The different geomechanical  
101 properties of outcropping rocks coupled with the inhomogeneous long-term updoming (De  
102 Guidi et al., 2014) of the volcano have produced a complex basement topography dominated  
103 by a 17 km-wide horseshoe-shaped depression beneath the eastern flank (Branca and Ferrara,  
104 2013). Such a complex basement topography would lead to the large-scale seaward motion of  
105 the eastern flank of Mt. Etna as clearly documented since the early 1980s (e.g. Borgia et al.,  
106 1992). At the surface, the unstable sector is defined by a 25 km-wide horseshoe-shaped region



107 which encompassing the sedimentary one is bounded by the “NE Rift - Pernicana fault and by  
108 the “South Rift - Mascalucia - Tremestieri - San Gregorio - Acitrezza fault system”,  
109 respectively on its NE and SE half (Figure 1). In addition, the presence of compressional  
110 structures (e.g. folds) at the toe of the continental margin as well as a prominent ESE lineament  
111 with prevailing right-lateral transpressive kinematics, located northward of Catania Canyon has  
112 recently been discovered, on the Etnean off-shore (Gross et al., 2015; Figure 1). Furthermore,  
113 active tectonics also occurs over the unstable sector and is distributed on a number of shallow  
114 faults such as the Timpe, the Santa Tecla, the Santa Venerina, the Fiandaca and the Nizzeti  
115 faults (Figure 1; Azzaro et al., 2012). The Timpe fault system consists of a 20 km long and 5  
116 km wide belt of mainly NNW to N extensional structures with well-developed morphological  
117 scarps; the Santa Tecla and Santa Venerina faults consist of two near parallel faults, which  
118 have a NW-SE trend and are characterized by right-lateral slips coupled with minor normal  
119 components. The Fiandaca fault is a NW-SE oriented right-lateral fault system with a normal  
120 component (Azzaro et al., 2012) which connects southward with the Nizzeti faults, a set of two  
121 NNE to NNW trending faults characterized by linear, up to 100 m high, cumulative scarps (De  
122 Guidi et al., 2018).

123 The definition of the basal sliding surface of Mt. Etna is widely debated and a number  
124 of different models have been proposed in the last 3 decades. For instance, Lo Giudice and  
125 Rasà (1992) postulate a shallow (~1.5 km) surface with a listric geometry located beneath the  
126 volcanic pile of Mt. Etna. Borgia et al. (1992) suggest an approximately 5-km-deep sub-  
127 horizontal west-dipping décollement. Tibaldi and Groppelli (2002) suggest the possibility of  
128 alternating or contemporaneous movements on both shallow and deep east-dipping slip  
129 surfaces under the effects of different source mechanisms. GPS-based models point to a sliding  
130 east-dipping surface located at a depth ranging from 0 to 5 km b.s.l. (see Palano 2016 and  
131 references therein).

132

### 133 **3.0 Data and modelling**

134

#### 135 *3.1 Geodetic data*

136 All available continuous GPS data on the eastern flank of Mt. Etna edifice were  
137 collected and analyzed in order to take into account the best spatially and temporally station  
138 coverage. To this aim we collected data from the following networks:

- 139 • Etn@net: this network is managed by the “Osservatorio Etneo” department of “Istituto  
140 Nazionale di Geofisica e Vulcanologia”. The setting up of this network began in  
141 November 2000 reaching a configuration of 13 stations in late summer of 2001 with  
142 daily sessions of about 8 hours. The network geometry was gradually upgraded over  
143 the years in order to cover all the slopes of the volcano edifice and to replace the sites  
144 destroyed by natural (lava flows) and human (vandalism) activities or affected by local  
145 instability, reaching the current configuration of 33 stations (blue dots in [Figure 1](#)). A  
146 continuous acquisition on sessions of 24 hours at all the stations was scheduled at least  
147 since early 2005. Pillars directly founded on consolidated bedrock represent the largest  
148 monument number.
- 149 • SiOrNet: this network is currently managed by the Geodetic Group of the Geological  
150 Survey of Italy-ISPRA and consists of 5 continuous GPS stations installed on some  
151 faults segments along the SE slope of Mt. Etna (yellow dots in [Figure 1](#)). The network  
152 was established in late 2005 and discontinuously worked until mid-2016. The  
153 functioning of the network was restored in late 2018 ([Pezzo et al., 2020](#)). Monuments  
154 consist on pillars directly founded on consolidated bedrock or steel masts anchored on  
155 concrete buildings.
- 156 • Italpos: this network is currently managed by Hexagon Geosystems  
157 (<https://hxgnsmartnet.com/it-it>). It was developed to support commercial applications,  
158 such as mapping and cadastral purposes and stations are characterized by a wide variety  
159 of different monument types. Pillars, or steel masts, anchored to buildings represent the  
160 largest number, while monuments directly founded on consolidated bedrock are present  
161 in minor percentage. Only 2 stations are installed on the volcano edifice (red dots in  
162 [Figure 1](#)); MASC was dismissed on early 2016.
- 163 • NetGEO: this network was developed by Geotop (<http://www.netgeo.it/>) since early  
164 2012. As the Italpos network, NetGEO was developed to support commercial  
165 applications. Monuments consist on pillars or steel masts, anchored to buildings. Such  
166 a network covers the volcano edifice with 2 stations installed on its eastern flank (black  
167 dots in [Figure 1](#)).

168 All collected data were processed using the GAMIT/GLOBK software ([Herring et al.,](#)  
169 [2018](#)) with IGS precise ephemerides. To improve the overall configuration of the network and  
170 tie the regional measurements to an external global reference frame, data coming from 15  
171 continuously operating IGS stations were introduced in the processing. We used the latest

172 absolute receiver antenna models by the IGS and we adopted the [Saastamoinen \(1972\)](#)  
173 atmospheric zenith delay models, coupled with the Global Mapping Functions ([Böhm et al.,](#)  
174 [2006](#)) for the neutral atmosphere. Estimated GPS daily time series and displacements for  
175 specified time intervals were referred to the “Etn@ref” reference frame (a local reference frame  
176 computed to isolate the Mt. Etna volcanic deformation from the background tectonic pattern;  
177 [Palano et al., 2010](#)).

178 From the visual inspection on the daily-based time series, we observed that at stations  
179 located along the lower eastern flank (group 1 with red time-series in [Figure 2](#)) each SSE  
180 produces or a sudden change (e.g. ELAC and MASC), or a more gradual change with respect  
181 to the linear trend of the time-series (e.g. EPOZ). Both changes occur with a finite duration and  
182 are characterized by rates that are faster than the long-term seaward motion of the unstable  
183 flank. The stations located on the middle sector of the eastern flank (group 2 with blue time-  
184 series in [Figure 2](#)), although showing a near continuous eastward motion, are also modulated  
185 by deformation related to inflation/deflation magmatic sources. The time-series of all these  
186 stations are also locally modulated by episodic creeping of the faults dissecting and/or  
187 bordering the unstable flank (see discussion). GPS stations externally located with respect the  
188 unstable flank (group 3 with time-series colored in black in [Figure 2](#)) are characterized by time  
189 series showing no deformation to gentle eastward motion. By inspecting the time-series of  
190 ACSA, SCAC, ELAC, MASC and EPOZ (null or very little influenced by the action of the  
191 magmatic sources) we detected 11 SSEs with duration grossly ranging from 2 to 67 days (see  
192 [Figure 2](#) and [Table 1](#)). On the analyzed time interval, the first SSE occurred in April 2006,  
193 while the last one in April 2016, therefore extending in time (back and forward) the SSE catalog  
194 previously defined in [Palano \(2016\)](#). Moreover, the time-series of the SiOrNet GPS stations  
195 allowed also to improve the detection of some SSEs (in term of SSE onset and related duration),  
196 leading to some differences with respect to the previous catalog. For each recognized SSE, we  
197 determine the amount of displacements by averaging site position in the 3 days preceding and  
198 following the event.

199

### 200 *3.2 Modelling*

201 The displacement fields were used to constrain isotropic half-space elastic inversion  
202 models. Although the faults dissecting and/or bordering the unstable flank might accommodate  
203 a fraction of deformation during each SSE, in the following we assumed that the slip occurs  
204 only along the basal sliding surface. Indeed, the current density of GPS stations on the eastern

205 flank of the volcano doesn't allow to properly differentiate the individual contribute of the  
206 basal sliding surface and the other active faults to the total ground deformation field.

207 The displacement field for SSEs lasting several days could contain a significant  
208 contamination from magmatic sources contemporaneously active. In particular, considering the  
209 SSEs with duration larger than 10 days, we observed that they occurred during inflation stages  
210 of the volcano, for which magmatic source parameters are already available in literature. We  
211 therefore subtracted the calculated effects of active magmatic sources from the observed  
212 displacement field to obtain the residual field which would correspond to the SSE contribute  
213 (see [Table 1](#)). Subtracted values range on average from ~3-5 mm for the stations located on the  
214 upper eastern flank to less than 0.5 mm for stations located along the coastal belt. Estimated  
215 residual displacements are reported in [Figure 3](#).

216 To determine the spatial distribution of slip for each SSE, we extended up to 36 x 36  
217 km and divided in 15 (along-strike) by 15 (along-dip) squared patches (dimension of 2.4 x 2.4  
218 km) a sliding surface similar to the one inferred in [Palano \(2016\)](#). We also fixed the dip of the  
219 sliding surface to 10° ([Table 2](#)). We used only the horizontal components of the deformation  
220 field being the vertical one too scattered among nearby stations. This choice is motivated by  
221 the lack of significant vertical variations related to each SSE on the GPS time series. To  
222 perform the elastic inversion models for each SSE we used the *GTdef* code ([Feng et al., 2012](#))  
223 which finds the optimal model parameters by using a linear least-squares solver scheme. In  
224 particular, *GTdef* seeks to solve the linear equation system relating the unknown slips ( $m$ ) to  
225 the observed deformation ( $d$ ) by applying a two-dimensional second-derivative (Laplacian)  
226 operator:

$$227 \begin{bmatrix} w^{-1}d \\ 0 \end{bmatrix} = \begin{bmatrix} w^{-1}G \\ k^2D \end{bmatrix} m \quad (1)$$

228  
229 where  $w$  is the diagonal matrix constructed from observation errors,  $G$  is the green function  
230 matrix,  $D$  is the second-order finite difference operator ([Jónsson et al., 2002](#)),  $k^2$  controls the  
231 weight imposed on the smoothing. The choice of smoothing leads to different model results  
232 where increasing smoothing values generally leads to an increase of model misfit. To determine  
233 the preferred model for each SSE, a trade-off curve between model misfit and roughness has  
234 been computed. The model misfit has been quantified through the chi-square value, while the  
235 average second-order finite difference sum of each patch has been used to indicate the model  
236 roughness  $\rho$  ([Jónsson et al., 2002](#)):

$$237 \rho = \frac{\sum_{il} p_{il}}{2N} \quad (2)$$

238

239 where  $p = Dm$  and  $N$  is the number of fault patches. The units of  $\rho$  are  $\text{cm}/\text{km}^2$ , indicating the  
240 average slip gradient (Jónsson et al., 2002). Our preferred models are reported in Figure 3 and  
241 are characterized by  $k$  ranging in the 4935 - 5755 interval (Figure S1).

242

## 243 4.0 Results and discussion

244 GPS stations installed on the lower unstable flank of Mt. Etna showed significant  
245 transient displacements (namely slow slip events) in their daily time-series position during a  
246 time interval of 10 years, from April 2006 to April 2016 (Figure 2). By a simple visual  
247 inspection of these time-series, we detected 11 SSEs with duration ranging from 2 to 67 days  
248 and with a very irregular average recurrence time of  $348 \pm 361$  days (Table 1). As above  
249 mentioned, we extended in time (back and forward) the SSE catalog previously defined in  
250 Palano (2016), improving also the definition of SSEs starting and temporal length, thank also  
251 to the GPS stations of the SiOrNet network. With respect to the previous catalog, we provided  
252 a better definition of starting and temporal length of SSE-02, SSE-03, SSE-05 and SSE-07  
253 (Table 1).

254

### 255 4.1 Surface deformation and modelled slip distribution

256 For each detected SSE, we estimated the surface deformation field which, in a  
257 successive step, was modelled to infer the spatial distribution of slip on a shallow sliding  
258 surface. Observed surface deformation (Figure 3) for most of the detected SSEs, mainly  
259 concentrates on the south-eastern edge of the on-shore unstable sector of the volcano edifice.  
260 Such a features is well evident for SSE-01, SSE-03, SSE-04, SSE-05, SSE-06, SSE-08, SSE-  
261 10 and SSE-11 (Figure 3), while SSEs involving the north-eastern edge are less frequent (SSE-  
262 07 and SSE-09). Therefore, the overall SSEs sequence highlights the existence of two distinct  
263 families of events involving the two contiguous sectors of the sliding flank as already suggested  
264 by Palano (2016), which occasionally slip together in large SSEs as observed during SSE-02.  
265 Moreover, the SiOrNet GPS stations allow to add new constrains to the deformation mode of  
266 the southern part of unstable flank of Mt. Etna. A primary key-feature is the differential motion  
267 observed along the Nizzeti faults, well captured by ACSA and SCAC stations (Figure 2 and  
268 Figure 3) and resulting in a general E-W extensional deformation. This feature is evident only  
269 in early SSEs since ACSA and SCAC worked until early 2014 and mid-2012, respectively.  
270 However, extensional deformation has been also observed by episodic measurements carried  
271 out along this sector of the volcano during November 2014 - April 2017 (De Guidi et al., 2018),

272 highlighting a significant role of the Nizzeti faults in controlling both the long- and the short-  
273 term patterns of deformation. A similar behavior has been also observed for the Timpe faults  
274 with a general eastward increase of displacements (Palano, 2016).

275 Some GPS stations located along the coastal belt (ELAC, MASC and ERIP) are  
276 characterized by large displacements, suggesting a causative source located in the closest off-  
277 shore region. Conversely, EPOZ and ETEC stations showed small to moderate displacements  
278 during each SSE, which is comparable in magnitude with the ones measured at stations located  
279 in the middle eastern flank. This aspect suggests that the magnitude of deformation is not  
280 controlled only by the “station-source” distance, but requires an additional external control.  
281 Since along the coastal belt, the sedimentary basement is located at very shallow depth (Branca  
282 and Ferrara, 2013), we evaluate a possible correlation between “displacement” and “volcanic  
283 cover thickness”. To this aim, for each SSE, we estimated both the daily displacement (i.e. the  
284 ratio between the total displacement and the event duration) and the volcanic cover thickness  
285 (by subtracting the sedimentary basement surface from the TINITALY digital elevation model;  
286 Figure 4a; Tarquini et al., 2007). Both estimated parameters are reported in Figure 4b: at a first  
287 glance, the average daily slip ( $s$ ) is inversely correlated with the volcanic cover thickness ( $v$ )  
288 and could be described as:

$$289 \quad s = -0.256 \log(v) + 1.964 \quad (3)$$

290 In particular, the average daily slip of ELAC, MASC and ERIP stations appears influenced by  
291 the thin volcanic cover (lesser than 5-10 meters), while on the other stations the volcanic cover  
292 thickness doesn't significantly affect the daily slip during each SSEs. Therefore, the pattern of  
293 deformation along the coastal area seems to be controlled by the volcanic cover thickness:  
294 thinner the volcanic cover is, larger the displacement rate will be. However, the physical  
295 significance of such correlation is unclear and requires additional studies and more data to be  
296 properly quantified and understood. The establishment of new continuous GPS stations along  
297 the coastal area, especially on these sectors characterized by thin volcanic cover would  
298 represent a good starting point for these future studies.

299 The finer model resolution as well as the large size of the planar source used in this  
300 study allowed to get a slip distribution on the basal sliding surface much better than the one  
301 achieved in Palano (2016), where the slip was not properly constrained at the edges of the  
302 adopted source because of its small size. Looking at the new results, for SSEs occurring more  
303 frequently, the slip distribution concentrates with values up to 6 cm on the southeastern sector  
304 of the sliding surface, ~10 km off-shore in correspondence of the prominent ESE lineament  
305 (Figure 3) discovered by (Chiocci et al., 2011). Such a sector also includes the segment of the

306 ESE lineament where an 8-day-long SSE occurred in May 2017 (temporally outside our GPS  
307 dataset), as observed by seafloor geodetic data (Urlaub et al., 2018). Regarding the SSEs  
308 involving the north-eastern edge of the unstable flank, the slip distribution on the modelled  
309 surface concentrates ~12 km off-shore beneath the Riposto Ridge (Figure 3), a structural high  
310 related to the Apennine thrust belt (Chiocci et al., 2011). The southern slope of the Riposto  
311 Ridge is marked by a ~16-km-long tectonic lineament mapped from ~6 km from the coast up  
312 to the flat-floor depression at the toe of the continental margin with a N102° attitude (Figure 1;  
313 Chiocci et al., 2011). This lineament would represent the off-shore prolongation of the most  
314 active splay of the Pernicana fault, however the lack of clear morphological evidences, doesn't  
315 support such a connection (Chiocci et al., 2011; Gross et al., 2015). It must be noted, however,  
316 that the seaward motion measured on-land, on the northeastern edge of the unstable flank, needs  
317 to be adsorbed on off-shore structures. Since the seismic data reported in Chiocci et al. (2011)  
318 and Gross et al. (2015) also doesn't show evidences of contractional structures in the near  
319 offshore, it is more realistic that the motion is transferred/adsorbed to the east, by the N102°  
320 lineament or by a not yet discovered sub-parallel fault.

321 The slip distribution allows us to estimate the geodetic magnitude of each SSE (Table  
322 1); by assuming a rigidity value of 15 GPa, estimated magnitude range between 5.4 (SSE-07)  
323 and 5.9 (SSE-01). Such a magnitude range is generally larger than the maximum magnitude  
324 (~5.2) estimated for earthquakes occurring at Mt. Etna in the last 200 years (Azzaro et al.,  
325 2015), therefore confirming the prevalent aseismic deformation of the unstable flank (Rasà et  
326 al., 1996).

327

#### 328 *4.2 General considerations and implications*

329 Previous InSAR-based studies (Solaro et al., 2010; Bonforte et al., 2011) defined  
330 geometry and kinematics of some blocks dissecting the unstable flank of the volcano, however  
331 a set of different deformation patterns observed in the last two decades depicts a complex block  
332 fragmentation of this flank, where, beside the slow slip events analyzed in this study, other  
333 different sources/mechanisms contributed at different spatial and temporal scales to its  
334 continuous seaward motion:

- 335 • The onset of energetic volcanic events such as the October 2002 - January 2003 eruption  
336 (Andronico et al., 2005) and the 24 December 2018 dyke intrusion (Pezzo et al., 2020)  
337 activated some hidden and blind fault segments, well highlighting the mentioned above  
338 complexity. For instance, the 2002-2003 eruption was accompanied by significant

339 ground deformation of the eastern flank mainly concentrated on its northern half, along  
340 the Pernicana fault and the Santa Tecla, Santa Venerina and Timpe faults, where few  
341 energetic seismic events (magnitude up to 4.4) also occurred (Neri et al., 2005).  
342 Conversely, the 24 December 2018 dyke intrusion led to extensive deformation of the  
343 eastern flank coupled with the occurrence of a shallow M4.9 earthquake on 26  
344 December 2018 striking the Fiandaca fault on the southern sector of the unstable flank  
345 (Pezzo et al., 2020).

- 346 • Significant post-eruption deformations of the unstable flank, have been also  
347 documented for ~6 months after the 2002-2003 (Palano et al., 2009) and 2018 (Pezzo  
348 et al., 2020) eruption onsets.
- 349 • Co-seismic displacements along the Pernicana fault related to  $M > 3.5$  earthquakes  
350 which generally produce large surface fractures and damage to man-made features (e.g.  
351 Azzaro et al., 1998; Bonforte et al., 2007; Guglielmino et al., 2011).
- 352 • Episodic or continuous creeping of the faults dissecting and/or bordering the unstable  
353 flank (Rasà et al., 1996).
- 354 • Vigorous and long lasting inflation/deflation episodes of the volcano edifice generally  
355 produce a pattern of deformation exponentially decreasing with the increase of distance  
356 from the magmatic source (Lisowski, 2008): this results in a significant deformation at  
357 the stations located at upper and middle elevations, and a very small motion at stations  
358 located along the coast (e.g. Aloisi et al., 2011; Bruno et al., 2012; Spampinato et al.,  
359 2015).

360 The temporal modulation of these sources/mechanisms led to substantial changes of the  
361 displacement rates on the unstable flank. For instance, horizontal rates from ~33 mm/yr to ~61  
362 mm/yr have been estimated for the 2003-2015 period for the southeastern and northern  
363 boundary of the sliding flank, respectively (Palano, 2016). Horizontal rates of ~28 mm/yr have  
364 been geodetically estimated during the 1997-2001 period (Palano et al., 2006) along the  
365 Pernicana fault, which are slight larger than the values estimated historically (Azzaro et al.,  
366 1998) and about an order of magnitude higher than the slip-rate estimated from geologic marker  
367 offsets (Azzaro et al., 2012). Geodetic vertical rates estimated for the 2003-2015 period depict  
368 a general subsidence with rates of ~15 mm/yr along the Pernicana fault, and of ~2-3 mm/yr  
369 along the faults bordering the southern boundary of the unstable flank (Palano, 2016). Such a  
370 general subsidence, although occurring at very low rates, can be also inferred by taking into  
371 account the available geologic estimations (Azzaro et al., 2012). Based on these observations,



372 the complex block fragmentation of the on-shore unstable flank of Mt. Etna led to a significant  
373 partition of the seaward motion among the steep faults bordering the blocks ([Figure 1](#)), where  
374 however, i) the northern half is generally characterized by the highest deformation rates and ii)  
375 most of the SSEs concentrated on the southeastern sector of the southern half. Conversely,  
376 according to the modelled slip distribution ([Figure 3](#)), the highest deformation rates occur on  
377 the southern half of the off-shore sector.

378 Our approach to model the surface deformation field of the unstable flank of Mt. Etna  
379 provides a good fit of the observed deformation, assuming however that it is entirely associated  
380 to slip along the basal sliding surface. Additional sources such as the faults bordering the  
381 unstable sector and the blocks inside it have been not considered in our approach, despite their  
382 proved role on accommodating/modulating a fraction of the observed deformation. Another  
383 limitation of our approach is that it models only static deformation patterns, while as mentioned  
384 above a number of sources/mechanisms contributes over different time spans to the observed  
385 deformation. Therefore, to properly constrain and quantify all the active sources modulating  
386 the seaward motion of the unstable flank of the volcano, a time-dependent modelling approach  
387 would represent a substantial onward step for future studies. A densification of the current  
388 continuous GPS network, especially across the active faults of the unstable flank as well as  
389 along the coastal area will greatly improve the observational dataset leading to more robust  
390 model set-up and on turn, to a better definition of the active sources of deformation. In addition,  
391 the use of techniques aimed to the displacement patterns match as the one proposed in  
392 [Montgomery-Brown et al. \(2009\)](#) will improve the detection of small events that may be close  
393 to the noise level in the GPS time series.

394 The seaward motion of the unstable flank would pose a potential threat to the whole  
395 region since large submarine landslides, or subaerial landslides plunging into the sea, could  
396 trigger tsunamis which on turn can hit the densely populated coasts surrounding the eastern  
397 Mediterranean Sea. A large tsunami hitting the eastern Mediterranean in early Holocene has  
398 been correlated with the collapse of the Valle del Bove ([Pareschi et al., 2006](#)), however such a  
399 correlation is highly debated ([Vigliotti, 2008](#)). Besides this event, no other tsunamis has been  
400 triggered by volcanic and/or flank collapse episodes at Mt. Etna volcano, at least since 6150  
401 BC ([Maramai et al., 2019](#)), therefore highlighting their very rare occurrence. This is not  
402 surprising and indeed, the occurrence of a large landslide at Mt. Etna, at least in the near future,  
403 is highly improbable because of the low slope of the volcano edifice ( $\sim 10^\circ$  on average) and the  
404 slow ( $\sim 61$  mm/yr) seaward motion of the unstable flank. The triggering of tsunamis by large

405 SSEs can be excluded too because of the low daily displacement rates (~2 mm/day) currently  
406 observed for each SSE from the continuous GPS stations (Figure 4).

407

## 408 **5.0 Conclusive remarks**

409 By inspecting the daily time series of the GPS stations located on the unstable flank of  
410 Mt. Etna we detected 11 SSEs occurred during the April 2006 - April 2016 time interval. Main  
411 conclusions can be summarized as following:

- 412 • Observed surface deformation for most of the detected SSEs, concentrates on the south-  
413 eastern edge of the unstable flank while SSEs involving the north-eastern edge are less  
414 frequent.
- 415 • The overall SSEs sequence highlights the existence of two distinct families of events  
416 involving the two contiguous sectors of the sliding flank, which occasionally slip  
417 together in large SSEs.
- 418 • The modelled slips put in evidence that both contiguous sectors extend ~10-12 km off-  
419 shore, on areas where tectonic lineaments such as the ESE (northward of Catania  
420 Canyon) and the N102° (along the southern slope of the Riposto Ridge) ones have been  
421 discovered in the last two decades.
- 422 • The faults dissecting the unstable flank control both the long- and the short-term  
423 patterns of seismic and aseismic deformation.
- 424 • The magnitude values of the SSEs sequence range in the 5.4-5.9 interval; these values  
425 are larger than the maximum observed one (at least in the last 200 years), evidencing  
426 as most of the deformation affecting the eastern flank occurs in aseismic mode.

427

428

## 429 **Acknowledgements**

430 We thank all colleagues involved in the maintenance and acquisition of GNSS data. We thank  
431 also Andrew V. Newman and his research group for sharing the *GTdef* code used in this study.

432 The figures were made using the Generic Mapping Tools v6.0.0 software (Wessel et al., 2019).

433 The GPS data used in this study have been analyzed in the framework of the Project  
434 “Paroxysmal volcanic events and seaward motion at Mt. Etna: an improved picture from a  
435 geodetic and seismological perspective” (Progetti di Ricerca Libera) funded by INGV.

436

## 437 **References**

438 Aloisi, M., et al. 2011. *Imaging the multi-level magma reservoir at Mt. Etna volcano (Italy)*.  
439 *Geophys. Res. Lett.* 38(16), L16306. <https://doi.org/10.1029/2011gl048488>.

440 Andronico, D., et al. 2005. A multi-disciplinary study of the 2002–03 Etna eruption: insights  
441 into a complex plumbing system. *Bull. Volcanol.* 67, 314–330.  
442 <https://doi.org/10.1007/s00445-004-0372-8>.

443 Azzaro, R., et al. 1998. Environmental Hazard of Capable Faults: The Case of the Pernicana  
444 Fault (Mt. Etna, Sicily. *Nat. Hazard.* 17(2), 147–162.  
445 <https://doi.org/10.1023/A:1008034422086>.

446 Azzaro, R., et al. 2012. The volcano-tectonic map of Etna volcano, 1:100.000 scale:  
447 morphotectonic analysis from high-resolution DEM integrated with geologic, active  
448 faulting and seismotectonic data. *It. J. Geosci. (Boll. Soc. Geol. It.)* 131 (1), 153–170.  
449 <https://doi.org/10.3301/IJG.2011.29>.

450 Azzaro, R., D'Amico, S., Tuvè, T., 2015. Seismic hazard assessment in the volcanic region of  
451 Mt. Etna (Italy): a probabilistic approach based on macroseismic data applied to volcano-  
452 tectonic seismicity. *Bull. Earth. Eng.* 14(7), 1813–1825. [https://doi.org/10.1007/s10518-015-](https://doi.org/10.1007/s10518-015-9806-2)  
453 [9806-2](https://doi.org/10.1007/s10518-015-9806-2).

454 Beavan, J., et al. 2007. Slow Slip Events on the Hikurangi Subduction Interface, New Zealand,  
455 in: Tregoning, P., Rizos, C. (Eds.), *Dynamic Planet*. International Association of Geodesy  
456 Symposia, vol 130. Springer, Berlin, Heidelberg, pp. 438–444.  
457 [https://doi.org/10.1007/978-3-540-49350-1\\_64](https://doi.org/10.1007/978-3-540-49350-1_64).

458 Böhm, J., et al. 2006. Global Mapping Function (GMF): A new empirical mapping function  
459 based on numerical weather model data. *Geophys. Res. Lett.* 33(7). <https://doi.org/10.1029/2005GL025546>.

461 Bonforte, A., et al. 2007. Ground deformation modeling of flank dynamics prior to the 2002  
462 eruption of Mt. Etna. *Bull. Volcanol.* 69(7), 757–768. [https://doi.org/10.1007/s00445-006-](https://doi.org/10.1007/s00445-006-0106-1)  
463 [0106-1](https://doi.org/10.1007/s00445-006-0106-1).

464 Bonforte, A., et al. 2011. Structural assessment of Mount Etna volcano from Permanent  
465 Scatterers analysis. *Geochem. Geophys. Geosyst.* 12(2).  
466 <https://doi.org/10.1029/2010GC003213>.

467 Borgia, A., Ferrari, L., Pasquarè G., 1992. Importance of gravitational spreading in the tectonic  
468 and volcanic evolution of Mount Etna. *Nature* 357(6375), 231–235.  
469 <https://doi.org/10.1038/357231a0>.

470 Branca, S., Ferrara, V., 2013. The morphostructural setting of Mount Etna sedimentary  
471 basement (Italy): Implications for the geometry and volume of the volcano and its flank  
472 instability. *Tectonophysics* 586, 46–64. <https://doi.org/10.1016/j.tecto.2012.11.011>.

473 Brudzinski, M. R., Allen, R. M., 2007. Segmentation in episodic tremor and slip all along  
474 Cascadia. *Geology* 35(10), 907–910. <https://doi.org/10.1130/G23740A.1>.

475 Bruno, V., et al. 2012. Ground deformations and volcanic processes as imaged by CGPS data  
476 at Mt. Etna (Italy) between 2003 and 2008. *J. Geophys. Res.: Solid Earth* 117(B7).  
477 <https://doi.org/10.1029/2011JB009114>.

478 Cannata, A., et al. 2018. Space-Time Evolution of Magma Storage and Transfer at Mt. Etna  
479 Volcano (Italy): the 2015–2016 Re-Awakening of Voragine Crater. *Geochem. Geophys. Geosyst.* 19, 471–495. <https://doi.org/10.1002/2017GC007296>.

481 Chiocci, F. L., et al. 2011. Continental margin large-scale instability controlling the flank  
482 sliding of Etna volcano. *Earth Planet. Sci. Lett.* 305(1–2), 57–64.  
483 <https://doi.org/10.1016/j.epsl.2011.02.040>.

484 De Guidi, G., Imposa, S., Scudero, S. et al. New evidence for Late Quaternary deformation of  
485 the substratum of Mt. Etna volcano (Sicily, Italy): clues indicate active crustal doming.  
486 *Bull. Volcanol.* 76, 816 (2014). <https://doi.org/10.1007/s00445-014-0816-8>

487 De Guidi, G., et al. 2018. The unstable eastern flank of Mt. Etna volcano (Italy): First results  
488 of a GNSS-based network at its southeastern edge. *J. Volcanol. Geotherm. Res.* 357, 418-  
489 424. <https://doi.org/10.1016/j.jvolgeores.2018.04.027>.

490 Dragert, H., Wang, K., James, T. S., 2001. A silent slip event on the deeper Cascadia  
491 subduction interface. *Science* 292(5521), 1525-1528.  
492 <https://doi.org/10.1126/science.1060152>.

493 Dragert, H., Wang, K., Rogers, G., 2004. Geodetic and seismic signatures of episodic tremor  
494 and slip in the northern Cascadia subduction zone. *Earth Planet. Space* 56 (12), 1143-  
495 1150. <https://doi:10.1186/BF03353333>.

496 Feng, L., et al. 2012. Active Deformation near the Nicoya Peninsula, Northwestern Costa Rica,  
497 Between 1996 and 2010: Interseismic Megathrust Coupling. *J. Geophys. Res.* 117,  
498 B06407, <https://doi:10.1029/2012JB009230>.

499 Foster, J. H., Lowry, A. R., Brooks, B. A., 2013. Fault frictional parameters and material  
500 properties revealed by slow slip events at Kilauea volcano, Hawaii. *Geophys. Res. Lett.*  
501 40, 6059-6063. <https://doi:10.1002/2013GL058234>.

502 Gross, F., et al. 2015. The limits of seaward spreading and slope instability at the continental  
503 margin offshore Mt Etna, imaged by high resolution 2D seismic data. *Tectonophysics*,  
504 <https://doi:10.1016/j.tecto.2015.11.011>.

505 Guglielmino, F., et al. 2011. Analysis of satellite and in situ ground deformation data integrated  
506 by the SISTEM approach: The April 3, 2010 earthquake along the Pernicana fault (Mt.  
507 Etna-Italy) case study. *Earth Planet. Sci. Lett.* 312(3-4), 327-336.  
508 <https://doi.org/10.1016/j.epsl.2011.10.028>.

509 Haines, J., Wallace, L. M., Dimitrova, L., 2019. Slow slip event detection in Cascadia using  
510 vertical derivatives of horizontal stress rates. *J. Geophys. Res.: Solid Earth* 124(5), 5153-  
511 5173. <https://doi.org/10.1029/2018JB016898>.

512 Herring, T.A., et al. 2018. Introduction to GAMIT/GLOBK, Release 10.7. Massachusetts  
513 Institute of Technology: Cambridge, UK. <https://www-gpsg.mit.edu>.

514 Hirose, H., et al. 1999. A slow thrust slip event following the two 1996 Hyuganada earthquakes  
515 beneath the Bungo Channel, southwest Japan. *Geophys. Res. Lett.* 26(21), 3237-  
516 3240. <https://doi.org/10.1029/1999GL010999>.

517 Ito, Y., et al. 2013. Episodic slow slip events in the Japan subduction zone before the 2011  
518 Tohoku-Oki earthquake. *Tectonophysics* 600, 14-26.  
519 <https://doi.org/10.1016/j.tecto.2012.08.022>.

520 Jónsson, S., et al. 2002. Fault slip distribution of the 1999 M w 7.1 Hector Mine, California,  
521 earthquake, estimated from satellite radar and GPS measurements. *Bull. Seismol. Soc.*  
522 *Am.* 92(4), 1377-1389. <https://doi.org/10.1785/0120000922>.

523 Linde, A., et al. 1996. A slow earthquake sequence on the San Andreas fault. *Nature* 383, 65-  
524 68. <https://doi.org/10.1038/383065a0>.

525 Lisowski, M., 2007. Analytical volcano deformation source models, in: *Volcano deformation*.  
526 Springer Praxis Books, Berlin, Heidelberg, pp. 279-304. [https://doi.org/10.1007/978-3-540-49302-0\\_8](https://doi.org/10.1007/978-3-540-49302-0_8).

528 Liu, Y., Rice, J. R., 2007. Spontaneous and triggered aseismic deformation transients in a  
529 subduction fault model. *J. Geophys. Res.* 112, B09404.  
530 <https://doi:10.1029/2007jb004930>.

531 Lo Giudice, E., Rasà, R., 1992. Very shallow earthquakes and brittle deformation in active  
532 volcanic areas: The Etnean region as an example. *Tectonophysics* 202, 257-268.  
533 [https://doi.org/10.1016/0040-1951\(92\)90111-I](https://doi.org/10.1016/0040-1951(92)90111-I).

534 Montgomery-Brown, E. K., Segall, P., Miklius, A., 2009. Kilauea slow slip events:  
535 Identification, source inversions, and relation to seismicity. *J. Geophys. Res.* 114,  
536 B00A03. <https://doi:10.1029/2008JB006074>.

- 537 Neri, M., et al. 2005. Contrasting triggering mechanisms of the 2001 and 2002–2003 eruptions  
538 of Mount Etna (Italy). *J. Volcanol. Geotherm. Res.* 144(1-4), 235-255.  
539 <https://doi.org/10.1016/j.jvolgeores.2004.11.025>.
- 540 Obara, K., Hirose, H., 2006. Non-volcanic deep low-frequency tremors accompanying slow  
541 slips in the southwest Japan subduction zone. *Tectonophysics* 417(1-2), 33-51.  
542 <https://doi.org/10.1016/j.tecto.2005.04.013>.
- 543 Palano, M., et al. 2006. Kinematics and strain analyses of the eastern segment of the Pernicana  
544 fault (Mt. Etna, Italy) derived from geodetic techniques (1997 - 2005). *Ann. Geophys.* 49,  
545 1105-1117.
- 546 Palano, M., Gresta, S., Puglisi, G., 2009. Time-dependent deformation of the eastern flank of  
547 Mt. Etna: after-slip or viscoelastic relaxation? *Tectonophysics* 473, 300-311,  
548 <https://doi:10.1016/j.tecto.2009.02.047>.
- 549 Palano, M., et al. 2010. Etn@ref: A geodetic reference frame for Mt. Etna GPS networks. *Ann.*  
550 *Geophys.* 53(4), 49-57. <https://doi:10.4401/ag-4879>.
- 551 Palano, M., 2016. Episodic slow slip events and seaward flank motion at Mt. Etna volcano  
552 (Italy). *J. Volcanol. Geotherm. Res.*, 324, pp. 8-14,  
553 <https://doi.org/10.1016/j.jvolgeores.2016.05.010>.
- 554 Palano, M., et al. 2017. Magma transport and storage at Mt. Etna (Italy): A review of geodetic  
555 and petrological data for the 2002-03, 2004 and 2006 eruptions. *J. Volcanol. Geotherm.*  
556 *Res.* 347, 149-164. <https://doi:10.1016/j.jvolgeores.2017.09.009>.
- 557 Pareschi, M. T., et al. 2006. Large submarine landslides offshore Mt. Etna. *Geophys. Res.*  
558 *Lett.* 33(13). <https://doi.org/10.1029/2006GL026064>.
- 559 Pezzo, G., et al. 2020. Flank sliding: A valve and a sentinel for paroxysmal eruptions and  
560 magma ascent at Mount Etna, Italy. *Geology*. <https://doi:10.1130/G47656.1>.
- 561 Rasà, R., Azzaro, R., Leonardi, O., 1996. Aseismic creep on faults and flank instability at  
562 Mount Etna volcano, Sicily. *Geol. Soc., Spec. Pub.* 110 (1), 179-192.  
563 <https://doi.org/10.1144/GSL.SP.1996.110.01.14>.
- 564 Rogers, G., Dragert, H., 2003. Episodic tremor and slip on the Cascadia subduction zone: The  
565 chatter of silent slip. *Science* 300, 5627, 1942-1943.  
566 <https://doi.org/10.1126/science.1084783>.
- 567 Rubin, A. M., 2011. Designer friction laws for bimodal slow slip propagation speeds.  
568 *Geochem. Geophys. Geosyst.* 12, Q04007. <https://doi:10.1029/2010gc003386>.
- 569 Saastamoinen, J., 1972. Atmospheric correction for the troposphere and stratosphere in radio  
570 ranging satellites. The use of artificial satellites for geodesy 15, 247-251.  
571 <https://doi.org/10.1029/GM015p0247>.
- 572 Segall, P., et al. 2010. Dilatant strengthening as a mechanism for slow slip events. *J. Geophys.*  
573 *Res.* 115, B12305. <https://doi:10.1029/2010jb007449>.
- 574 Solaro, G., et al. 2010. Anatomy of an unstable volcano from InSAR: Multiple processes  
575 affecting flank instability at Mt. Etna, 1994-2008. *J. Geophys. Res.* 115, B10405.  
576 <https://doi:10.1029/2009JB000820>.
- 577 Spampinato, L., et al. 2015. Multiparametric study of the February–April 2013 paroxysmal  
578 phase of Mt. Etna New South- East crater. *Geochem. Geophys. Geosyst.* 16(6), 1932-  
579 1949. <https://doi.org/10.1002/2015GC005795>.
- 580 Tarquini, S., Isola, I., Favalli, M., Battistini, A., 2007. TINITALY, a digital elevation model of  
581 Italy with a 10 m-cell size (Version 1.0). Istituto Nazionale di Geofisica e Vulcanologia  
582 (INGV).
- 583 Tibaldi, A., Groppelli, G., 2002. Volcano-tectonic activity along structures of the unstable NE  
584 flank of Mt. Etna (Italy) and their possible origin. *J. Volcanol. Geotherm. Res.* 115, 277–  
585 302. [https://doi:10.1016/S0377-0273\(01\)00305-5](https://doi:10.1016/S0377-0273(01)00305-5).

586 Urlaub, M., et al., 2018. Gravitational collapse of Mount Etna's southeastern flank. *Sci.*  
587 *Adv.* 4(10), eaat9700. <https://doi.org/10.1126/sciadv.aat9700>.  
588 Vigliotti, L., 2008. Comment on "Lost tsunami" by Maria Teresa Pareschi et al. *Geophys. Res.*  
589 *Lett.* 35(2). <https://doi.org/10.1029/2007GL031155>.  
590 Wech, A. G., Bartlow, N. M., 2014. Slip rate and tremor genesis in Cascadia. *Geophys. Res.*  
591 *Lett.* 41(2), 392-398. <https://doi.org/10.1002/2013GL058607>.  
592 Wessel, P., Luis, J. F., Uieda, L., Scharroo, R., Wobbe, F., Smith, W. H. F., & Tian, D. (2019).  
593 The Generic Mapping Tools version 6. *Geochemistry, Geophysics, Geosystems*, 20,  
594 5556-5564. <https://doi.org/10.1029/2019GC008515>

595  
596

### 597 **Figure Captions**

598 **Figure 1.** Simplified tectonic map of Mt. Etna and its eastern off-shore. Bathymetry is from  
599 [www.emodnet-bathymetry.eu](http://www.emodnet-bathymetry.eu). GPS stations covering Mt. Etna volcano are reported as colored  
600 points. Abbreviations are as follows: PF, Pernicana fault; TFS, Timpe fault system; SVF, Santa  
601 Venerina fault; STF, Santa Tecla fault; FF, Fiandaca fault; NF, Nizzeti fault system; TF,  
602 Trecastagni fault; MTF, Mascalucia-Tremestieri fault; ESEL, ESE lineament. Inset: sketch  
603 map of eastern Sicily; AMC, Apennine-Maghrebian chain; HF, Hyblean Foreland; GCF, Gela-  
604 Catania Foredeep.

605

606 **Figure 2.** On the right, time series of the East component of continuous GPS stations installed  
607 on the lower and middle eastern flank of Mt. Etna. GPS time series are colored according to  
608 their main features. GPS time series showing sudden change on their linear trend or a change  
609 with respect to their long-term trend are colored in red (group 1). GPS time series showing a  
610 continuous eastward motion, superposed by inflation/deflation deformation are colored in blue  
611 (group 2). GPS time series showing no deformation to gentle eastward motion and externally  
612 located with respect the unstable flank are colored in black (group 3).

613

614 **Figure 3.** Observed (blue arrows) and modelled (red arrows) surface displacements related to  
615 each detected SSE. Slip distributions on modelled decollement surface are also reported. See  
616 Table 1 for additional details.

617

618 **Figure 4.** a) Estimated volcanic cover thickness computed as the height difference between the  
619 TINITALY digital elevation model (Tarquini et al., 2007) and the sedimentary basement  
620 surface (Branca and Ferrara, 2013). b) Correlation between volcanic cover thickness and daily  
621 displacement (see text for details).

622

623 **Figure S1.** Trade-off curve between roughness and chi-square misfit (see text for details) for  
624 each modelled SSE. The preferred model is chosen in the inflection corner of the curve (yellow  
625 star). The corresponding  $k$  value is also reported.

626

### 627 **Table Captions**

628 **Table 1.** Catalog of slow slip events identified in this study. For each SSE, the duration, the  
629 geodetic moment (GM) and the estimated magnitude ( $M_w$ ) are also reported. The deformation  
630 related to active magmatic sources has been removed from the displacement field of SSE-01,

631 SSE-02, SSE-03, SSE-05 and SSE-09 by adopting the source parameters available in literature  
632 (Pal17, [Palano et al., 2017](#); Alo11, [Aloisi et al., 2011](#); Spa15, [Spampinato et al., 2015](#); Can18,  
633 [Cannata et al., 2018](#)).

634

635 **Table 2.** Parameters of the modelled sliding surface. The position (latitude, longitude and  
636 depth) indicates the top-center of the modelled surface. Depth (positive downward) is referred  
637 to the mean elevation of GPS stations used in this study, namely 1100 m above sea level.

638

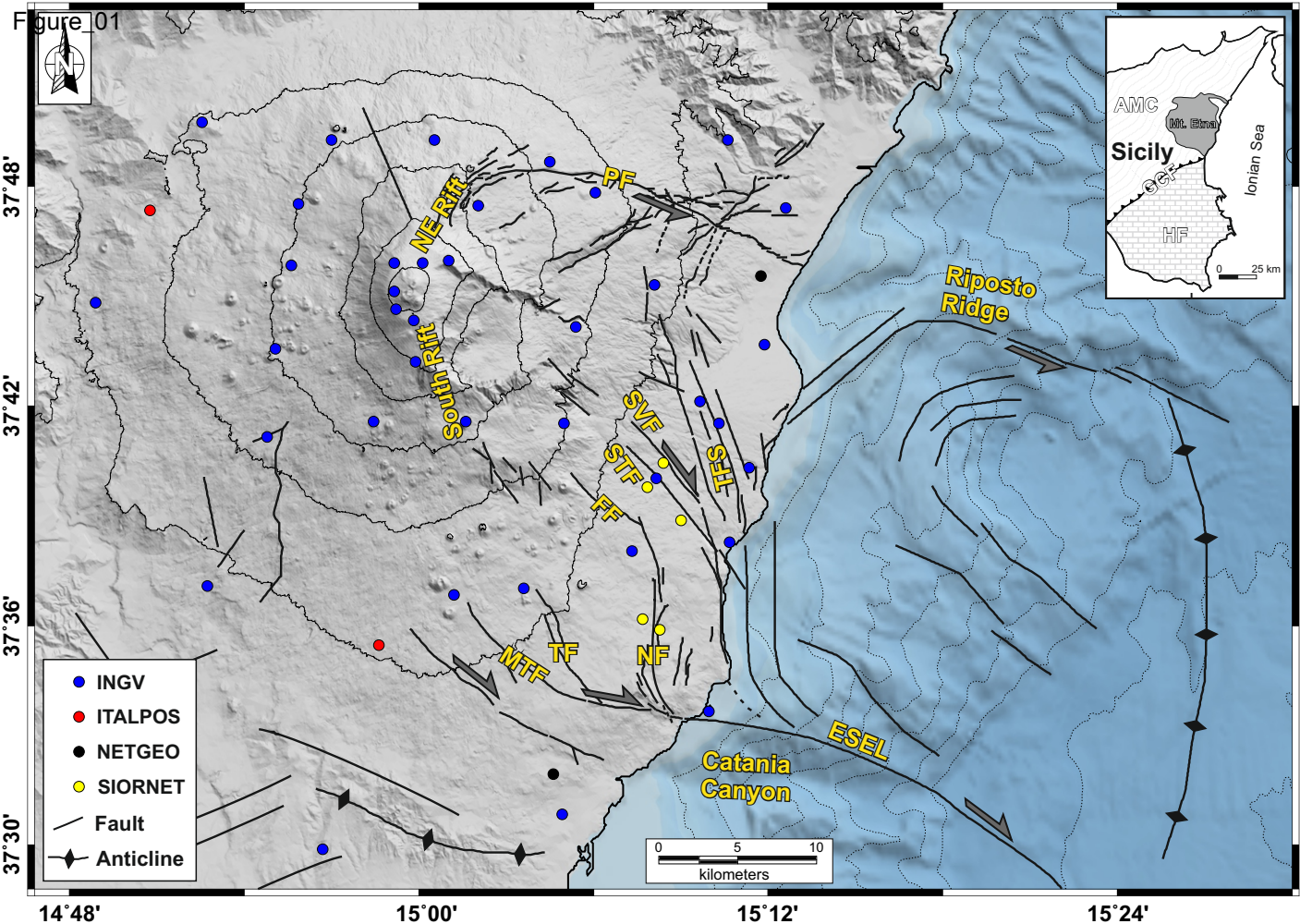
Longitude (°)	15.03
Latitude (°)	37.70
Depth (m)	500
Length (km)	36.0
Width (km)	36.0
Azimuth (°)	13.5
Dip (°)	10.0

**Table 2.** Parameters of the modelled sliding surface. The position (latitude, longitude and depth) indicates the top-center of the modelled surface. Depth (positive downward) is referred to the mean elevation of GPS stations used in this study, namely 1100 m above sea level.

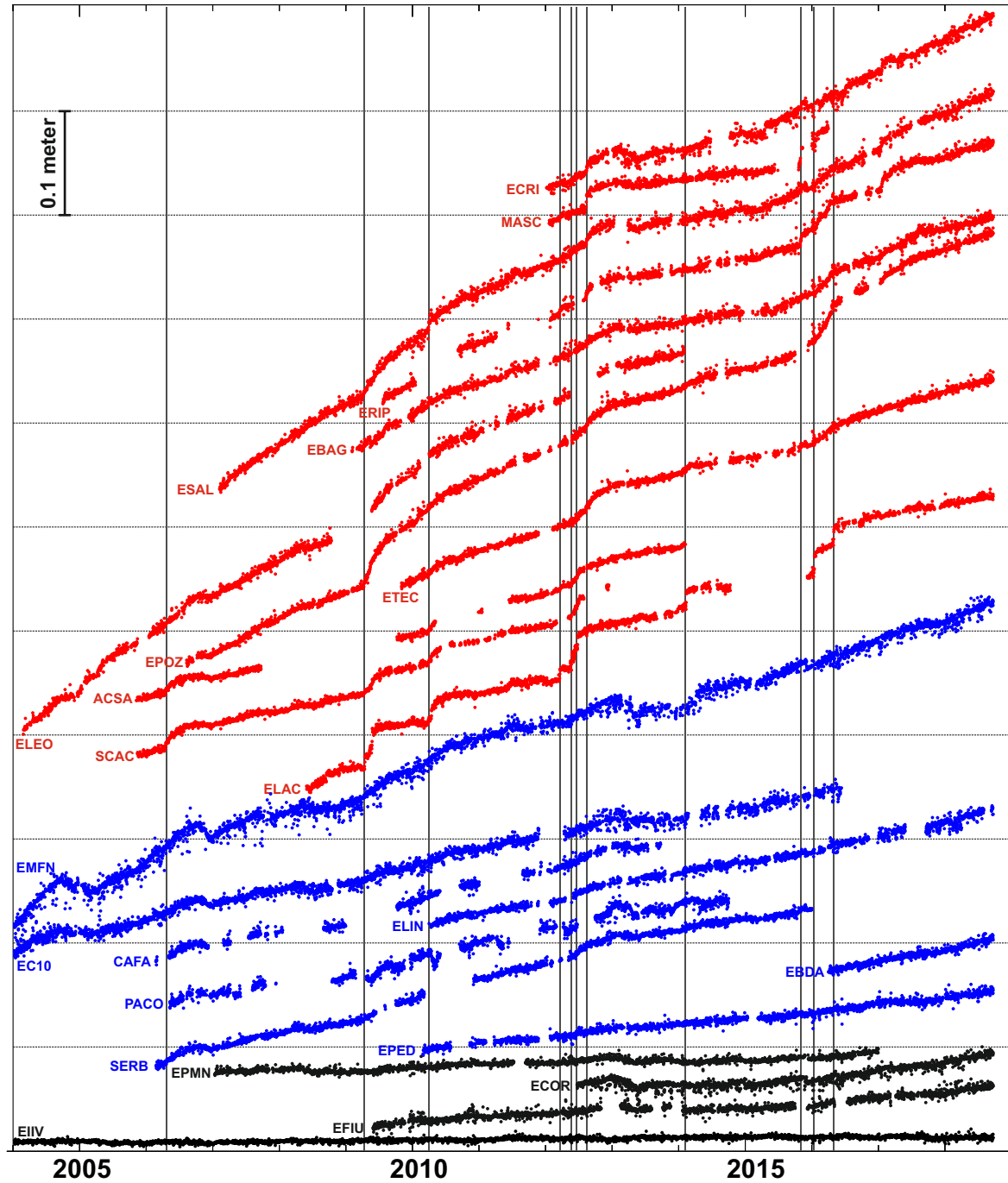
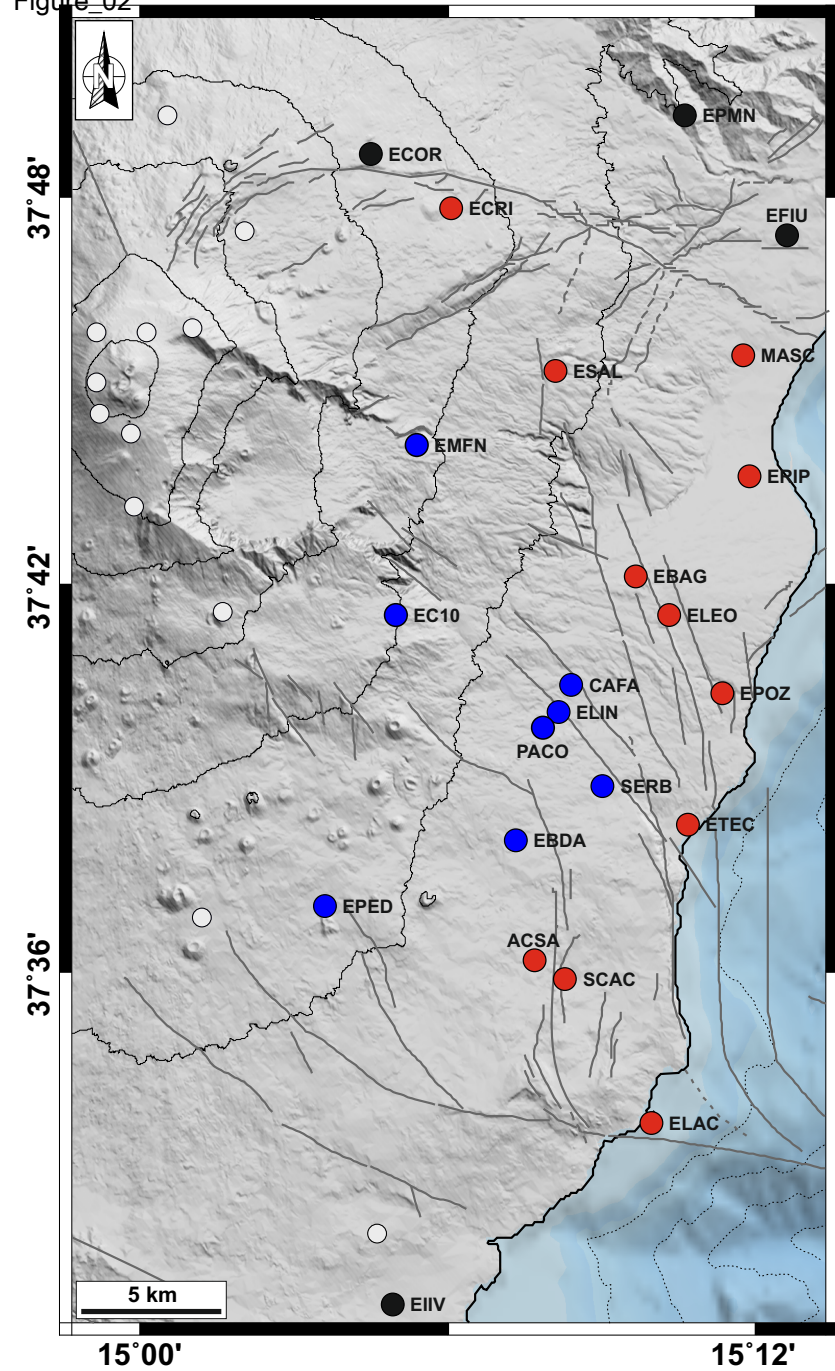


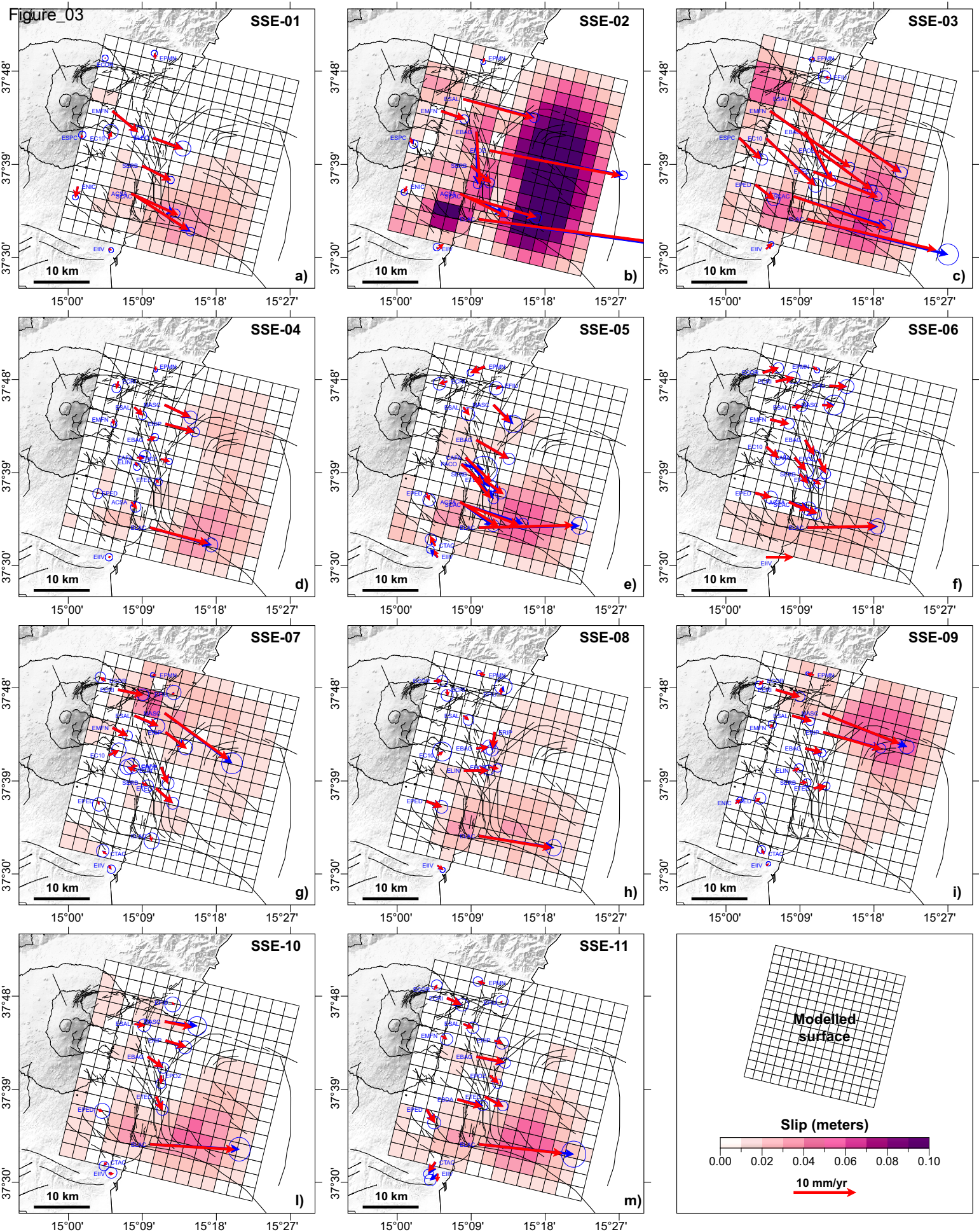
SSE_Id	Event date	Duration (days)	GM (Nm)	M <sub>w</sub>	Notes
SSE-01	16/04/2006	13	$1.84 \cdot 10^{17}$	5.48	Pal17
SSE-02	13/04/2009	42	$8.60 \cdot 10^{17}$	5.92	Alo11
SSE-03	27/03/2010	67	$3.86 \cdot 10^{17}$	5.69	Alo11
SSE-04	16/03/2012	5	$2.15 \cdot 10^{17}$	5.52	
SSE-05	15/05/2012	29	$2.42 \cdot 10^{17}$	5.56	Spa15
SSE-06	24/06/2012	4	$1.56 \cdot 10^{17}$	5.43	
SSE-07	10/08/2012	4	$1.49 \cdot 10^{17}$	5.42	
SSE-08	10/02/2014	2	$1.95 \cdot 10^{17}$	5.49	
SSE-09	26/10/2015	12	$2.52 \cdot 10^{17}$	5.57	Can18
SSE-10	14/01/2016	3	$2.45 \cdot 10^{17}$	5.56	
SSE-11	28/04/2016	5	$2.34 \cdot 10^{17}$	5.55	

**Table 1.** Catalog of slow slip events identified in this study. For each SSE, the duration, the geodetic moment (GM) and the estimated magnitude (M<sub>w</sub>) are also reported. The deformation related to active magmatic sources has been removed from the displacement field of SSE-01, SSE-02, SSE-03, SSE-05 and SSE-09 by adopting the source parameters available in literature (Pal17, [Palano et al., 2017](#); Alo11, [Aloisi et al., 2011](#); Spa15, [Spampinato et al., 2015](#); Can18, [Cannata et al., 2018](#)).



Figure\_02









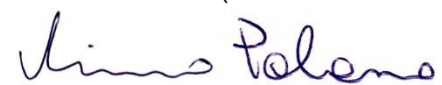
[Click here to access/download](#)

**Supplementary material for online publication only**  
**Figure\_S01.pdf**



All the authors know and concur with the submission of this manuscript to **Tectonophysics** journal and declare no conflict of interests.

Mimmo Palano (on behalf all the authors)

A handwritten signature in blue ink that reads "Mimmo Palano". The signature is written in a cursive style with a large initial 'M' and a long horizontal stroke at the end.